JOURNAL OF APPLIED CRYSTALLOGRAPHY

ISSN: 1600-5767
journals.iucr.org/j

Quantification of passivation layer growth in inert anodes for molten salt electrochemistry by *in situ* energy-dispersive diffraction

Matthew R. Rowles, Mark J. Styles, Ian C. Madsen, Nicola V. Y. Scarlett, Katherine McGregor, Daniel P. Riley, Graeme A. Snook, Andrew J. Urban, Thomas Connolley and Christina Reinhard

J. Appl. Cryst. (2012). **45**, 28–37

Journal of
Applied
Crystallography
ISSN 0021-8898

Received 27 June 2011
Accepted 24 October 2011

Quantification of passivation layer growth in inert anodes for molten salt electrochemistry by *in situ* energy-dispersive diffraction

Matthew R. Rowles,[a,b,c]* Mark J. Styles,[b,c] Ian C. Madsen,[a,c] Nicola V. Y. Scarlett,[a,c] Katherine McGregor,[a,c] Daniel P. Riley,[d] Graeme A. Snook,[a,c] Andrew J. Urban,[a,c] Thomas Connolley[e] and Christina Reinhard[e]

[a]CSIRO Process Science and Engineering, PO Box 312, Clayton South, Victoria 3169, Australia, [b]Department of Mechanical Engineering, University of Melbourne, Parkville, Victoria 3010, Australia, [c]CSIRO Future Manufacturing Flagship, Private Bag 33, Clayton South MDC, Victoria 3169, Australia, [d]Institute of Materials Engineering, ANSTO, Locked Bag 2001, Kirrawee DC, New South Wales 2232, Australia, and [e]Diamond Light Source Ltd, Harwell Science and Innovation Campus, Didcot, Oxfordshire OX11 0DE, UK. Correspondence e-mail: matthew.rowles@csiro.au

An *in situ* energy-dispersive X-ray diffraction experiment was undertaken on operational titanium electrowinning cells to observe the formation of rutile (TiO_2) passivation layers on Magnéli-phase (Ti_nO_{2n-1}; $n = 4$–6) anodes and thus determine the relationship between passivation layer formation and electrolysis time. Quantitative phase analysis of the energy-dispersive data was undertaken using a crystal-structure-based Rietveld refinement. Layer formation was successfully observed and it was found that the rate of increase in layer thickness decreased with time, rather than remaining constant as observed in previous studies. The limiting step in rutile formation is thought to be the rate of solid-state diffusion of oxygen within the anode structure.

1. Introduction

Molten salt electrolysis has become a key technology in the field of extractive metallurgy. It is used extensively in the production of light metals such as aluminium, lithium and magnesium (Habashi, 1997), and is being investigated (Gianatta, 2000; Kraft, 2004; Fray, 2008) as a potential replacement for the Kroll (1940) process for titanium production. Currently, graphitic carbon anodes and cell linings (Jiao & Fray, 2010) are used in titanium electrowinning research, with many unwanted outcomes. Carbon is an undesirable electrode material as it (i) reacts with the electrolyte and anode products, (ii) contaminates the electrowon metal, (iii) requires constant replacement, and (iv) is a source of anthropogenic CO_2. As a result of these effects, process control is significantly complicated. In contrast to carbon, an ideal inert anode is not consumed during the electrolysis, does not react with the anode products and therefore does not contaminate the electrowon metal, and hence has a much lower impact on process control. However, inert anodes are prone to failure as, in practice, they are attacked by the electrolyte and by the oxygen evolved at the anode. In order to develop these new anode materials (Pawlek, 2008, 2010), a more detailed understanding of the structural and chemical changes that lead to their failure is needed.

Traditionally, characterization of materials involved in electrochemical investigations conducted at elevated temperatures in molten salts has relied upon *ex situ* or *post mortem* methodologies. These methods can be problematic as conventional analysis techniques typically require some form of sample preparation, which can range from simply allowing the sample to cool, to more invasive procedures such as cutting and polishing. All of these procedures may change the sample, thus affecting the analysis and hence the understanding of how it interacts with its environment.

Few *in situ* techniques have been developed for molten salt systems owing to the particularly challenging nature of the sample environment. A 'see-through cell' has been developed by McGregor *et al.* (2007), which uses a transparent quartz crucible for the direct observation of both the anode and the cathode in a molten calcium chloride electrolyte at 1223 K. Although this has given many insights into anode behaviour, the electrochemistry of the system is compromised, as quartz is soluble in the electrolyte and passivates the anode surface.

In order to monitor surface changes on operational electrodes, an extremely penetrating probe is required. Scarlett *et al.* (2009) developed a methodology for the analysis of energy-dispersive X-ray diffraction data that allows for the nondestructive phase identification and quantification, *via* the Rietveld (1969) method, of the internal components of an operational electrochemical cell. This methodology was developed using static (*i.e.* non-operating) cells which had been prepared earlier, cooled to room temperature (frozen) and removed from the furnace prior to analysis. This approach was undertaken in order to determine whether or not the detection limits of such a method would be adequate for the

study of an operational electrochemical cell. The success of that experiment (Rowles *et al.*, 2011) has led to the current work, in which operating anodes have been examined using energy-dispersive diffraction data collected during the course of an electrochemical experiment.

The cells used in the present study simulate those that would be used for the production of titanium metal from a TiO_2 cathode using a Magnéli-phase (Andersson *et al.*, 1957) material [Ebonex (Hayfield, 1983), containing Ti_nO_{2n-1}, where n ranges from 4–6] as a model 'inert' anode. Ebonex was used as a model anode as (i) the phase changes that occur in this material during electrolysis have been substantially characterized *ex situ* (McGregor *et al.*, 2006), allowing findings made during *in situ* experimentation to be corroborated by *ex situ* data, (ii) it does not contaminate the electrolyte or cathode, and (iii) it remains dimensionally stable. The electrochemical cell preparation is detailed by Scarlett *et al.* (2009) and is summarized here: The electrodes are immersed in a molten $CaCl_2$ electrolyte at ~1223 K, electrolysis is conducted and the anode is eventually oxidized to nonconducting TiO_2 (rutile) after ~7 h of electrolysis, depending on the size of the anode. The electrode reactions for the process are given by

$$\text{Cathode:}\quad TiO_2 + 4e^- \rightarrow Ti + 2O^{2-}; \tag{1}$$

$$\text{Anode:}\quad 2O^{2-} \rightarrow O_2 + 4e^-; \tag{2}$$

$$\text{Overall:}\quad TiO_2 \rightarrow Ti + O_2. \tag{3}$$

These reactions were probed through the application of energy-dispersive X-ray diffraction (Giessen & Gordon, 1968), using high-energy polychromatic synchrotron radiation to allow the examination of a particular volume element within a relatively large sample (Barnes *et al.*, 2000; Scarlett *et al.*, 2009; Russenbeek *et al.*, 2011; Cernik *et al.*, 2011). An advantage of this technique compared to monochromatic instruments is the relatively simple incident beam optics, resulting in much higher X-ray intensities at the sample, and a simple exit path to the detector.

Both conventional angle-dispersive diffraction and energy-dispersive diffraction work by satisfying Bragg's law,

$$\lambda = 2d\sin\theta, \tag{4}$$

where λ is the wavelength of the incident radiation, d is the interplanar spacing of the diffracting crystal and 2θ is the diffraction angle. In most laboratory and synchrotron powder diffractometers, λ is monochromatic and 2θ is measured in order to determine d. This experimental arrangement is referred to here as angle-dispersive diffraction (ADD).

Energy is related to wavelength by

$$E = hc/\lambda = 12.398/\lambda, \tag{5}$$

where E is the energy of the incident radiation in keV, h is Planck's constant (4.136×10^{-18} keV s^{-1}), c is the speed of light (2.998×10^{18} Å s^{-1}) and λ is the wavelength, in ångströms, associated with that energy. Substitution of equation (4) into equation (5) allows the d spacing to be determined using a fixed θ position and variable energy,

$$E = 6.199/(d\sin\theta), \tag{6}$$

where d is given in ångströms and 2θ is the angle between the incident beam and the detector slit (Fig. 1). This experimental arrangement is referred to here as energy-dispersive diffraction (EDD).

2. Experimental

2.1. Diffraction instrumentation

In energy-dispersive mode, Beamline I12 at the Diamond Light Source receives high-energy white X-rays from a 4.2 T wiggler with a usable energy range of 30–150 keV. The diffracted X-rays are measured using a semi-annular array of 23 liquid-nitrogen-cooled germanium energy-sensitive detectors 2 m from the sample position at an angle of ~5° 2θ to the incident beam (see Fig. 2). The diffracted beam was collimated by two slit systems: a 150 µm semi-annular slit 551 mm from the sample position and a series of 200 µm slits immediately in front of each detector. As this system is an energy-dispersive detector, the measured intensities will include peaks arising from fluorescence as well as crystalline diffraction, which must be accounted for in any data analysis.

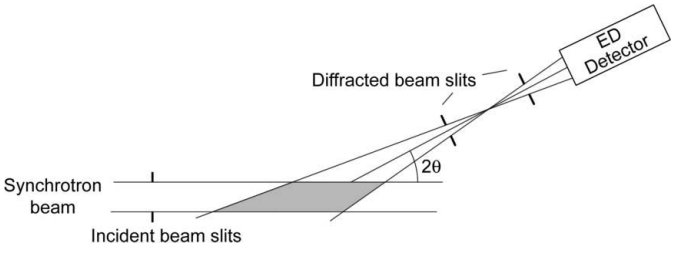

Figure 1
The experimental arrangement for energy-dispersive diffraction. A parallel X-ray beam is incident on the sample, and a collimated energy-dispersive detector at an angle 2θ collects diffraction information from the shaded area.

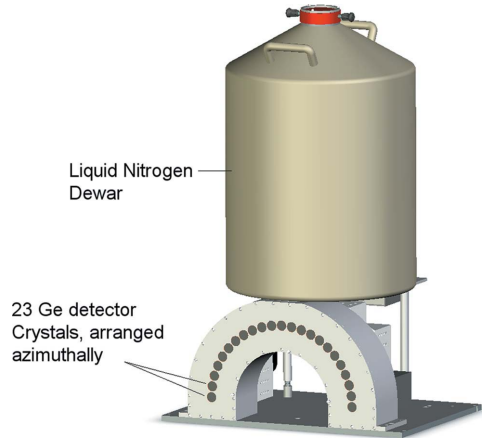

Figure 2
The semi-annular detector array used for EDD at Beamline I12, Diamond Light Source. Each detector incorporates a 200 µm slit, which, when coupled with the other 150 µm slit just after the sample, acts as a collimator in the fashion of Fig. 1.

The volume of the sample from which diffraction information is obtained is referred to as the 'gauge' or 'active' volume and defined by the intersection of the paths of the incident beam and the detector collimators. This intersection creates a lozenge-shaped (Häusermann & Barnes, 1992) volume of investigation (Fig. 1), which is fixed in space and through which the sample is scanned to obtain diffraction information from its different parts. The length of the lozenge is a function of the incident beam height, h, the angle of diffraction, 2θ, the angular acceptance of the detector collimator, α, and the distance, e, from the sample to the collimator, as given in equation (7) (Rowles, 2011):

$$L = h[\cot(2\theta - \alpha) + \cot(2\theta - \alpha)] + e\sin\alpha[\operatorname{cosec}(2\theta - \alpha) + \operatorname{cosec}(2\theta + \alpha)]. \quad (7)$$

2.2. Sample environment

A detailed account of the design and construction of the sample environment is given by Styles *et al.* (2012) and is summarized below.

2.2.1. Furnace. The furnace used to heat the electrochemical cells is shown schematically in Fig. 3. It is a 2.4 kW vertical tube furnace, accommodating reaction vessels up to 60 mm in diameter and capable of heating samples to a maximum of 1373 K. Prior testing indicated that the sample temperature was maintained within 1 K of the set point.

The furnace design permits unobstructed passage of X-rays through the furnace, with a conical diffracted beam port allowing diffraction data to be collected out to a minimum of 10° 2θ. The furnace body is mounted inside a machined aluminium frame, which allows for the accurate, repeatable positioning of the electrochemical cell (§2.2.2), and hence the electrode stalk and anode, within the X-ray beam (see Fig. 4).

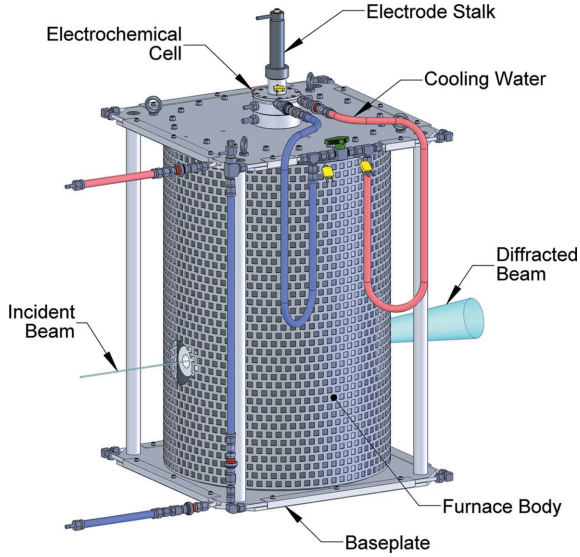

Figure 3
Schematic of the furnace.

2.2.2. Electrochemical cells. (i) Electrolyte. High-purity grade calcium chloride ($CaCl_2$; Sigma Aldrich), containing 0.2–0.5 wt% CaO, was dried in a laboratory furnace by ramping the material to 393 K at 5 K min^{-1} and holding at this temperature for 60 min, followed by further heating to 643 K at 0.11 K min^{-1} and holding at this temperature for 12 h. Upon cooling to 473 K, the $CaCl_2$ was transferred to an Ar-atmosphere glove box, where it was allowed to cool to room temperature. It was subsequently placed into several single-use plastic bottles in batches of 320 g and sealed to prevent hydration of the $CaCl_2$.

The $CaCl_2$ was used for multiple electrolysis runs, significantly improving the utilization of available synchrotron beamtime. The electrode response was continually monitored by both detection of fluctuations in the cell voltage and visual inspection of used electrode stalks, for indications of impurities in the melt. The cell was replaced with a freshly prepared one as necessary.

(ii) Electrode stalk. To facilitate efficient sample changes, the anode and cathode samples were both mounted on a single 'electrode stalk' (Styles *et al.*, 2012). This device consists of a concentric tube arrangement (shown in Fig. 4) in which the current pathways are electrically insulated from one another by alumina tubes.

Ebonex was obtained from Atraverda Ltd (UK) in plate form (150 mm diameter, 2–3 mm thick). Rectangular anodes,

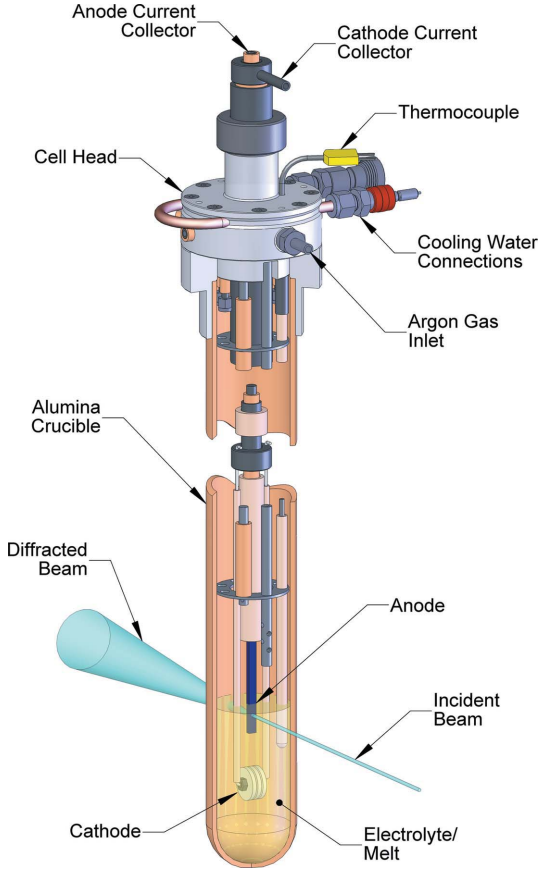

Figure 4
Schematic of the cell head, crucible and electrode stalk.

3 mm thick by 5 mm wide by 75 mm long, were cut from the purchased plate. These were held in place on the electrode stalk by wrapping 15 mm of one end in copper foil and inserting it between the two tines of a specially designed anode holder. The cathode consisted of three sintered TiO_2 pellets (approximately 1 g each). These were supported on a short length of alumina-sheathed stainless steel rod which was suspended about 20 mm below the anode on a bent Inconel wire (see Fig. 4).

(iii) Cell head and crucible. The water-cooled cell head (Fig. 4) consists of a quick-connect-style port for the electrode stalk, a thermocouple well, a gas supply and exhaust fittings, and three additional electrode terminals. The quick-connect port was designed to locate the anode sample within 1 mm of the central axis of the cell, while allowing accurate adjustment of anode height and angular position, minimizing the time required to locate the anode with the X-ray beam.

The cell body consists of a closed-end alumina tube bonded into an aluminium cap. The internal diameter of the crucible accommodates the sample stalk with sufficient radial clearance for ancillary devices such as thermocouples, gas supply tubes and reference electrodes.

(iv) Electrolyses. Electrolyses were conducted by applying a constant current supplied by a PAR Model 362 Scanning Potentiostat fitted with a PAR Model 365 current booster (maximum 10 A). The current was ramped at 1.75 Ah^{-1} until the operating current was reached. Cell voltage, current and bath temperature were measured and recorded every second for the duration of the experiment.

The electrolyses were conducted under an argon cover gas (ultra high purity, 99.999%) in a $CaCl_2$ electrolyte at a temperature of 1223 K and an applied current of 0.7 A for up to 7 h or until anode failure. Anodes were dipped into the melt to give an exposed area of approximately 3.5 cm^2. The anode was allowed to rest, immersed in the bath, for one hour to ensure that the electrode was in a stable state prior to electrolysis. It is during this time that the melt creeps up the electrode, as well as soaking into the electrode pores (Snook *et al.*, 2009). To investigate the effect of current and therefore oxygen supply on anode degradation, one electrolysis was conducted at half-current, *i.e.* 0.35 A. An anode was deemed to have failed when the cell resistance increased to above $\sim$7 Ω.

The Ar cover-gas flow was taken from the crucible through a series of NaOH water baths in order to remove any $CaCl_2$ and HCl from the gas prior to venting to the beamline gas extraction system.

2.3. Standards and synchrotron data collection

2.3.1. Standards. EDD data were collected on a series of standard materials in order to characterize the instrument with respect to (*a*) the X-ray intensity distribution as a function of energy, (*b*) the detector FWHM as a function of energy and (*c*) the detector channel-to-energy conversion. The standards used were lanthanum hexaboride (NIST SRM 660a), silicon (NIST SRM 640a) and the suite comprising the IUCr Commission on Powder Diffraction Round Robin Sample 1 (Madsen *et al.*, 2001), which consisted of a range of compositions of the three-phase mixture corundum (Al_2O_3), fluorite (CaF_2) and zincite (ZnO). Synthetic bauxite (Scarlett *et al.*, 2002) was used as a test sample to determine the accuracy and precision of the quantification technique. All standards were presented to the beam as loose powders in 1 mm quartz glass capillaries.

2.3.2. Synchrotron data collection. EDD data were collected over an energy range of approximately 6–160 keV, with useful intensities from 30 to 120 keV. Diffraction data from all 23 detectors were obtained as a function of time from a single position on each sample. Standard data sets were collected for 600 s. *In situ* data sets were collected for 60 s, with a 5 s delay between consecutive data sets for the duration of the experiment. The arrangement of the anode in the incident beam is shown in Fig. 4. The active volume for each diffraction pattern was 1 $\times$ 1 mm perpendicular to the beam and $\sim$15 mm long in the direction of the incident beam. The anode was positioned in the approximate centre of this active volume by scanning the anode through the incident beam and observing the intensity of the diffraction peaks – when the peaks where at a maximum, the anode was deemed to have been positioned correctly. The anode occupied only 30% of the active volume, resulting in an increased background contribution to the diffraction pattern from the melt. However, a larger beam gave greater flexibility in anode alignment and resulted in a larger diffracting volume, ensuring that a representative powder pattern could be collected, outweighing any disadvantages from an increase in observed pattern background.

In separate electrolysis runs, data were collected above or below the surface of the electrolyte to observe the effect of electrolyte absorption on the diffracted intensities. The data collected above the melt surface still produced information regarding the anode performance (see §3.2) as the liquid electrolyte crept up the outer surface of the anode, enabling electrolysis to occur (Snook *et al.*, 2009).

2.4. Data analysis

2.4.1. Energy-dispersive modelling. The analysis methodology used in this work was developed by Scarlett *et al.* (2009) and is summarized here. There are four fundamental differences between EDD and ADD which restrict the use of the Rietveld methodology for the analysis of EDD data: (i) the variance of structure factors as a function of energy, (ii) a nonlinear distribution of intensity in the incident beam as a function of energy, which is further modified by (iii) a nonlinear detector response, and (iv) the preferred absorption of lower-energy X-rays by the sample, further skewing the energy distribution. These factors complicate the calculation of a model diffraction pattern, as most Rietveld packages do not have the ability to model these effects.

As our preferred approach is to retain the raw data in its 'as collected' form, and to develop appropriate models in the pattern calculation step, the data analysis methodology taken here was to adopt a structure-based Rietveld (1969) refine-

ment using *TOPAS* (Bruker, 2009), to model the pattern directly on the energy scale by using algorithms that embody equation (6). The diffraction data were input into *TOPAS* as channel number *versus* intensity and internally converted to an energy scale by assuming a linear conversion from channel to energy using conversion factors determined from data obtained from known standards. This conversion was transparent to the data analysis methodology.

A parameter was defined to represent the wavelength, which was dependent upon the fixed detector angle as given in equation (4), and this was used to calculate energy in terms of *d* spacing *via* equation (5). The energy returned was then used internally by *TOPAS* to determine the structure factors used in the intensity calculations. Peak positions were then determined directly on an energy scale from unit-cell dimensions and symmetry.

Intensity corrections were dealt with in three parts. The first part related to the intensity distribution in the incident beam and the detector efficiency, and was determined by a combination of standard measurements and theoretical calculations. The second part dealt with X-ray absorption by the sample and other materials in the beam path, and was refined along with other sample-related parameters. The final part was the Lorentz factor for white-beam radiation. An additional correction may also be made for the polarization of the incident beam.

The intensity distribution was modelled using a lognormal function,

$$I_{\text{incident}} = \frac{a}{E}\exp\left(-\frac{1}{2}\left\{\frac{\ln[(E-b)/c]}{d}\right\}^2\right), \tag{8}$$

where E is the energy and a, b, c and d are refinable parameters relating to the height, cut-off energy, position and FWHM of the peak, respectively. The initial values of these parameters were gained through fitting the energy spectrum of the wiggler as calculated by *XOP* (Sánchez Del Río & Dejus, 1997). The detector response, I_{detector}, was included as a polynomial interpolation of the efficiency data reported by Tzeng *et al.* (1976); this polynomial was not refined.

$$\begin{aligned} I_{\text{detector}} = {} & 0.808735 + 2.80319 \times 10^{-3}E + 1.59884 \times 10^{-4}E^2 \\ & - 3.78446 \times 10^{-6}E^3 + 2.28942 \times 10^{-8}E^4 \\ & - 4.36174 \times 10^{-11}E^5. \end{aligned} \tag{9}$$

The intensity variation attributable to absorption by all components of the furnace, crucible, electrolyte and sample in the incident and diffracted X-ray beam was modelled with an exponential function,

$$I_{\text{absorption}} = \exp\left[-\sum_{i=1}^{n}\mu_i(E)t_i\right], \tag{10}$$

where the thickness, t, of each component, i, was a refinable parameter and the mass absorption coefficient, μ, was taken from the NIST database (Hubbell & Seltzer, 2004). The implementation of this equation takes into account the presence of absorption edges.

The variation in intensity due to the Lorentz effect for white-beam radiation has been derived by Lange (1995):

$$I_{\text{Lorentz}} = (\lambda/\sin\theta)^2. \tag{11}$$

A general polarization correction for the diffracted beam was derived by Azároff (1955). It has been adapted for the polarization of a white X-ray beam, *i.e.* no monochromator, and is given as

$$I_{\text{polarization}} = \frac{(\cos^2 2\theta\cos^2\kappa + \sin^2\kappa)P + (\cos^2 2\theta\sin^2\kappa + \cos^2\kappa)}{1+P}, \tag{12}$$

where κ is the azimuthal angle[1] (see Fig. 2) and P is the degree of polarization of the incident beam in the plane of the storage ring, 1 being unpolarized, 0 being totally polarized.

The calculated peaks were scaled by the product of these functions

$$I_{\text{corrected}} = I_{\text{incident}}I_{\text{detector}}I_{\text{absorption}}I_{\text{Lorentz}}. \tag{13}$$

The shapes of peaks in the diffraction patterns were modelled using a pseudo-Voigt function. The instrument contribution to the peak shapes in the EDD data was limited to Gaussian broadening with a linear energy-dependent term and constant Lorentzian broadening. The full widths at half-maxima, β, are given in equations (14) and (15),

$$\beta_{\text{Gaussian}} = m_{\text{G}}E + c_{\text{G}}, \tag{14}$$

$$\beta_{\text{Lorentzian}} = c_{\text{L}}, \tag{15}$$

where the slope and intercepts were determined from refinements on LaB_6 and Si. The Scarlett *et al.* method has been extended to allow explicitly for a sample contribution to the peak shapes by modelling crystallite size [equation (16)] and strain [equation (17)] as given by Gerward *et al.* (1976),

$$\beta_{\text{size}} = 6.199/(L\sin\theta), \tag{16}$$

$$\beta_{\text{strain}} = 2sE, \tag{17}$$

where the crystallite size, L, is given in ångströms. Broadening due to crystallite size was assumed to be solely Lorentzian, whilst that due to strain, s, was solely Gaussian.

Contributions from fluorescence peaks arising from the Pb and W detector shielding and collimators, as well as La, where necessary, were modelled. Fluorescence peak positions and relative intensities were fixed (Kortright & Thompson, 2001), and a scale parameter for each peak group (*e.g. K* shell) was introduced as a refinable parameter. The peaks were modelled using a pseudo-Voigt function, with the FWHM and Lorentzian component constrained to be the same for each peak group. The presence of fluorescence peaks sometimes introduced a discontinuity in the background. To overcome this, separate background functions were used, as necessary, to model the background on either side of the fluorescence peaks.

[1] For $\kappa = 0^\circ$, this expression reduces to the classic polarization expression $(P\cos^2 2\theta + 1)/(1+P)$, where P is given by $\cos^n 2\theta_{\text{M}}$ for the case of monochromatic radiation.

It was also necessary to model the contribution of detector escape peaks from both diffraction and fluorescence peaks. The contribution was incorporated by introducing a second phase with identical parameters to the parent phase, but with an independent scale factor, and whose peaks were shifted to lower energies by a constant offset of 9.9 keV, the value of the unresolved Ge $K\alpha$ emission.

2.4.2. Rietveld refinement. To determine the intensity characteristics, diffracted beam angles and FWHM contribution of the detectors, the refinable parameters in equations (6), (8), (14) and (15) were determined using the standard suite comprising round robin sample 1 (Madsen *et al.*, 2001), as well as LaB_6 and Si. The parameters were refined using a surface analysis approach described by Stinton & Evans (2007). In this analysis methodology, all the models for all the standards are refined simultaneously, and all instrument (incident intensity, detector FWHM, channel-to-energy) and structural parameters (unit-cell parameters, crystallite size and strain) are constrained to be identical across all models. Individual phase scale factors were allowed to refine independently. During this step, the intensity variations attributable to absorption [equation (10)] were constrained by the mass absorption coefficients and the known weight fractions of each of the samples in order to isolate the contribution of the instrument. Fig. 5 shows the functional forms of the intensity correction term and its components for LaB_6. The approach taken here allows at least part of the function to be constrained by measurable instrumental parameters and the remainder to have some relationship to physical parameters of the sample. The separation of the instrument and sample-related parameters allows the analysis of materials with widely differing absorption characteristics without having to recalibrate the intensity corrections. Only data from the central detector were analysed.

When refining the data collected from the electrolytic cells, the instrumental components were fixed at those refined from the standard suite. The refinements were again undertaken using a surface analysis approach as outlined by Stinton & Evans (2007). A single value of melt thickness, crucible thickness and escape peak energy offset were refined over the entire data set. The structures used in this analysis were rutile (Restori *et al.*, 1987), Ti_5O_9 (Le Page & Strobel, 1982*a*) and Ti_6O_{11} (Le Page & Strobel, 1982*b*). The scale factors of the three phases were allowed to refine independently, as were the lattice parameters of rutile. The lattice parameters of Ti_5O_9 were constrained to a single value each and refined over the surface. The a and β lattice parameters of Ti_6O_{11} were allowed to refine independently, as their values were stable under refinement, while the remainder were constrained to a single value each and refined over the surface. The rutile and Ti_6O_{11} crystallite sizes were allowed to refine independently, while the crystallite size for Ti_5O_9 was set to be equal to the corresponding value for Ti_6O_{11}. The sample thickness was allowed to refine independently. No atom positions were refined.

Relative phase abundances were derived using the *ZMV* algorithm of Hill & Howard (1987):

$$w_i = s_i(ZMV)_i \Big/ \sum_{j=1}^{n} s_j(ZMV)_j, \qquad (18)$$

where w_i is weight fraction of phase i, s_i is the Rietveld scale factor of that phase, *ZMV* is the 'calibration constant' derived from the unit-cell mass (ZM) and volume (V), and n is the number of phases in the calculation.

The quality of the fit of the calculated pattern to the data was assessed by the weighted pattern R factor (Young, 1993, p. 22):

$$R_{\rm wp} = \left[\sum_{m=1}^{M} w_m (Y_{{\rm obs},m} - Y_{{\rm calc},m})^2 \Big/ \sum_{m=1}^{M} w_m Y_{{\rm obs},m}^2 \right]^{1/2}, \qquad (19)$$

where $Y_{{\rm obs},m}$ and $Y_{{\rm calc},m}$ are the observed and calculated intensities at data point m, M is the number of data points, and w_m is the weighting given to data point m, which was equal to $1/Y_{{\rm obs},m}$.

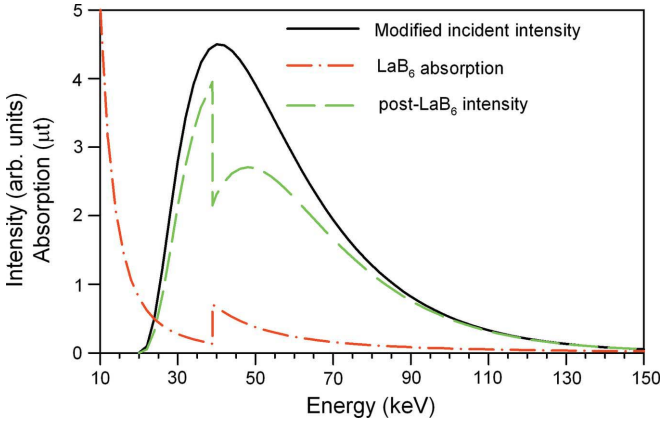

Figure 5
General form of the intensity corrections showing the lognormal incident intensity curve as modified by the detector response, the absorption curve of a sample of LaB_6 and the resultant intensity after absorption from the sample. Note the effect of the La K-absorption edge on the intensity distribution in the diffracted/transmitted beam.

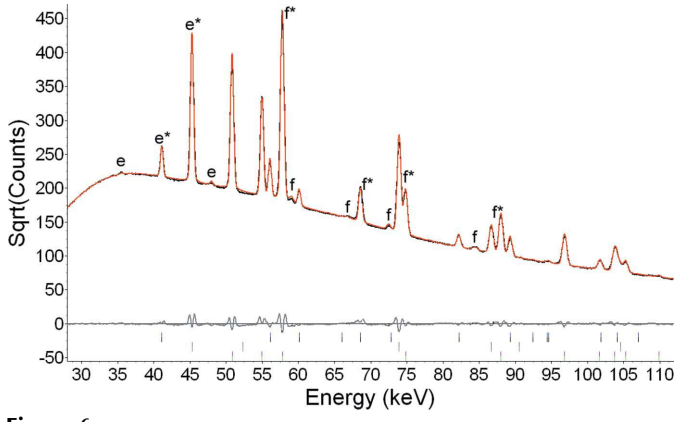

Figure 6
Results of the Rietveld refinement on sample 1*g* from the IUCr CPD round robin. It was necessary to model both fluorescence (f) and detector escape peaks (e) to obtain a satisfactory fit. The stars denote peaks that are coincident with diffraction peaks.

Table 1
Comparison of the quantitative phase analysis of EDD data collected from the IUCr CPD Sample 1 with the known amounts (weighed).

	Corundum (wt%)		Fluorite (wt%)		Zincite (wt%)	
Sample	Weighed	EDD	Weighed	EDD	Weighed	EDD
1*a*	1.15	1.08	94.81	95.31	4.04	3.61
1*b*	94.31	95.55	4.33	3.51	1.36	0.94
1*c*	5.04	4.97	1.32	1.38	93.59	93.64
1*d*	13.53	13.55	53.58	53.86	32.89	32.59
1*e*	55.12	58.45	29.62	27.78	15.25	13.77
1*f*	27.06	24.36	17.72	18.50	55.22	57.14
1*g*	31.37	31.94	34.42	34.12	34.21	33.94

Table 2
Comparison of the quantitative phase analysis of EDD data collected from the IUCr CPD synthetic bauxite with the known amounts (weighed).

Note that kaolinite parameters were fixed to give an adequate whole-of-sample refinement as explained in §3.1.

Phase	Weighed (wt%)	EDD (wt%)
Anatase	2.00	2.39
Boehmite	14.93	12.28
Goethite	9.98	8.16
Haematite	10.00	9.87
Quartz	5.16	6.69
Gibbsite	54.90	57.49
Kaolinite	3.02	3.02

3. Results and discussion

3.1. Standards

Fig. 6 shows part of the results of the surface refinement of the standards suite. For clarity, only Sample 1*g* has been shown. Table 1 shows the results of quantification of the sample 1 suite using this method and Table 2 shows the application of the derived instrument model to the analysis of the 'unknown' synthetic bauxite. The results show good agreement between the weighed and measured values for each of the samples considered, showing that the derived instrument model is sound and can be confidently applied to the *in situ* data. Note that, in this refinement, all kaolinite parameters were fixed at known values, as the main peak of kaolinite occurs at the lower-energy cut-off of the incident beam, and did not allow for a stable refinement because of its extremely low intensity.

3.2. Electrochemical cells

Accumulated diffraction patterns collected centrally on the anode are shown in Fig. 7: (*a*) 7 mm above the surface of the melt at full current, (*b*) 3 mm below the surface of the melt at full current and (*c*) 7 mm above the surface of the melt at half current. For the data collected above the melt (Figs. 7*a* and 7*c*), the diffraction peaks for each phase are clearly visible, and Pb and W fluorescence lines do not contribute significantly to the pattern, although they were included in the model. It was necessary to include secondary structures as described above in order to account for detector escape peaks arising from the intense diffraction peaks. For the data collected below the melt (Fig. 7*b*), the diffraction peaks for each phase are less visible owing to the absorption of lower-energy X-rays by the melt. Pb and W fluorescence lines now contribute significantly

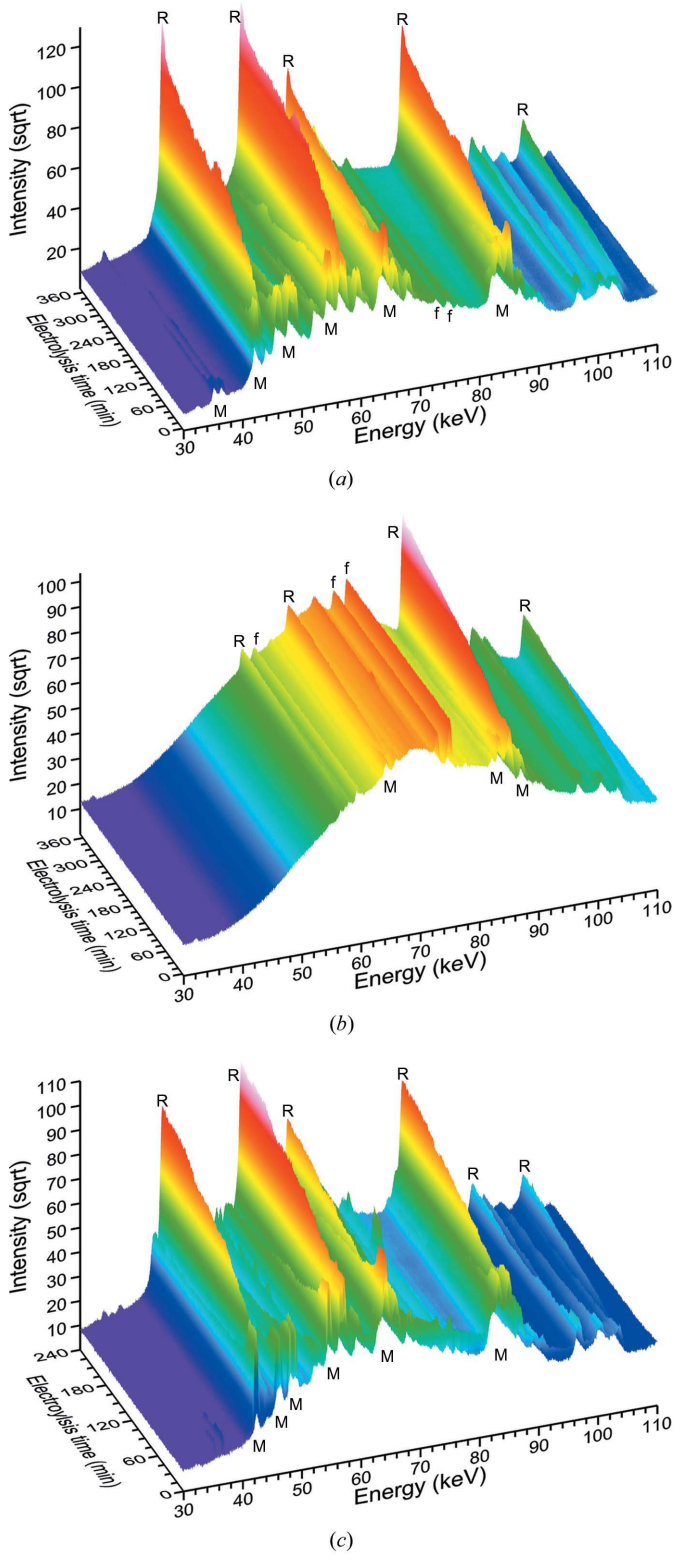

Figure 7
Accumulated EDD patterns for data collected (*a*) above the melt, (*b*) below the melt and (*c*) above the melt at half current density. The main rutile (R), Magnéli (M) and fluorescence (f) peaks are marked.

to the pattern, as they are unaffected by the absorption of the melt because they are present in the instrument, not the sample or cell. In particular, the Pb $K\beta_1$ line, which is directly under the rutile 211 peak, became apparent. It was not necessary to include secondary structures in order to account for escape peaks, as the intensity of the parent peaks were reduced owing to absorption in the electrolyte, and the resultant escape peaks were not of any significance.

The calculated diffraction patterns fit the collected data quite well (see Fig. 8). The inclusion of fluorescence and detector escape peaks accounted for the vast majority of the peak misfits in the model. The crystallite sizes as calculated from equation (16) agree with those values previously calculated from standard ADD. No strain broadening was identified. No preferred orientation was seen in any of the phases. There was no significant variation in the lattice parameters of the Magnéli phases with electrolysis time. The lattice parameters of rutile increased rapidly to a constant value as rutile formed on the anode.

Fig. 8 shows a single diffraction pattern, and the calculated model, from data collected (*a*) above and (*b*) below the melt.

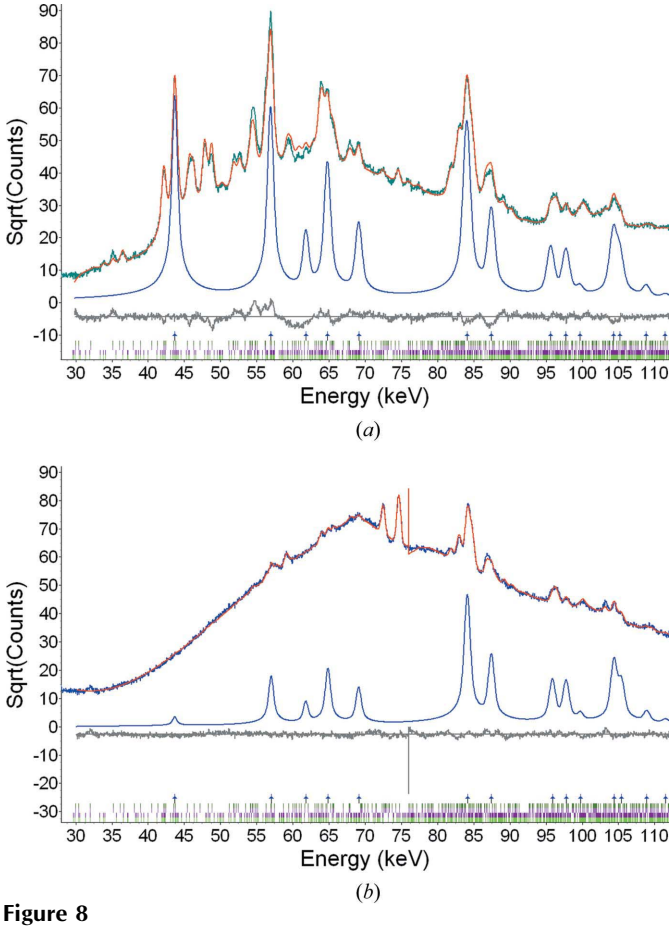

Figure 8
Comparison of the data collected and the calculated model (*a*) above (R_{wp} = 6.39) and (*b*) below (R_{wp} = 3.47) the melt surface. In both instances, the calculated pattern for rutile is shown, indicating the effect of X-ray absorption on the diffracted intensities. The data presented show the three phases – rutile, Ti_5O_9 and Ti_6O_{11} – present at approximately 33 wt% each. The spike in the difference plot in (*b*) at ∼76 keV is an artefact brought on by the models used for the background.

Immediately obvious is the difference in intensity distribution due to the absorption of lower-energy X-rays by the melt. The model used was able to account for this difference through the change of a single parameter relating to the thickness of the $CaCl_2$. The only phases observed in the two anodes were the Magnéli phases Ti_5O_9 and Ti_6O_{11} and rutile. No evidence was observed for the formation of $CaTiO_3$ seen in previous electron microprobe studies (McGregor *et al.*, 2006), which is to be expected, as the thin $CaTiO_3$ layer would represent less than 1 wt%: probably below the detection limits for this synchrotron technique. This is in accord with the findings on the static cells when examined both *in situ* (Scarlett *et al.*, 2009) and *post mortem* (Rowles *et al.*, 2011).

Fig. 9 shows the results of quantitative phase analysis of the diffraction data collected (*a*) above the melt at full current, (*b*) below the melt at full current and (*c*) above the melt at half current. It can be seen that in all systems rutile forms at the expense of both Magnéli phases equally. Some rutile is present initially in Figs. 9(*b*) and 9(*c*), indicating that exposure to the melt without any applied current may result in oxidation of the anode surface, although this may be an artefact of the model due to the low quality of the data. The Ti_5O_9/Ti_6O_{11} ratio present in Fig. 9(*c*) differs significantly from those in Figs. 9(*a*) and (*b*). Many different analysis strategies were employed to reconcile this difference and it remained as an observable difference in the quantitative phase analysis (QPA).

The similarities in the QPA above and below the melt surface show that it is possible to obtain meaningful *in situ* diffraction data without the X-ray beam having to penetrate the bulk of the melt, as the melt creeping up the anode surface (Snook *et al.*, 2009) allows electrolysis to occur out of the bulk melt. This also mitigates the detrimental effect of X-ray absorption on the resultant diffraction patterns.

The QPA results can be used to calculate an approximate thickness of the rutile layer forming on each of the anodes (Scarlett *et al.*, 2009; Rowles *et al.*, 2011). In the case of this data collection regime, where the incident beam is narrower than the anode, the rutile layers can be represented as a two-dimensional flat plate that grows symmetrically along one dimension from the outside of the anode towards the centre. An estimate of the layer thickness may be calculated from the QPA of the anodes' diffraction patterns as

$$T_{\text{rutile}} = T_{\text{anode}} \frac{1}{2} \frac{w_{\text{R}}/\rho_{\text{R}}}{w_{\text{R}}/\rho_{\text{R}} + w_{\text{T5}}/\rho_{\text{T5}} + w_{\text{T6}}/\rho_{\text{T6}}}, \qquad (20)$$

where ρ is the crystallographic density of the phase modified by a packing ratio of the phase, w is the quantitative phase analysis of the phase and T_{anode} is the thickness of the anode. The subscripts R, T5 and T6 denote rutile, Ti_5O_9 and Ti_6O_{11}, respectively. The factor of $\frac{1}{2}$ accounts for the contribution from both sides of the anode. Fig. 10 shows the results of these calculations assuming a packing ratio of 1 (Rowles *et al.*, 2011).

The amount of oxygen produced at the anode in the half-current experiment is half that produced in the full-current experiment, but the thickness curves (Fig. 10) reveal that rutile is forming at the same rate. From these observations, the limiting factor in the growth of rutile is more likely to be the

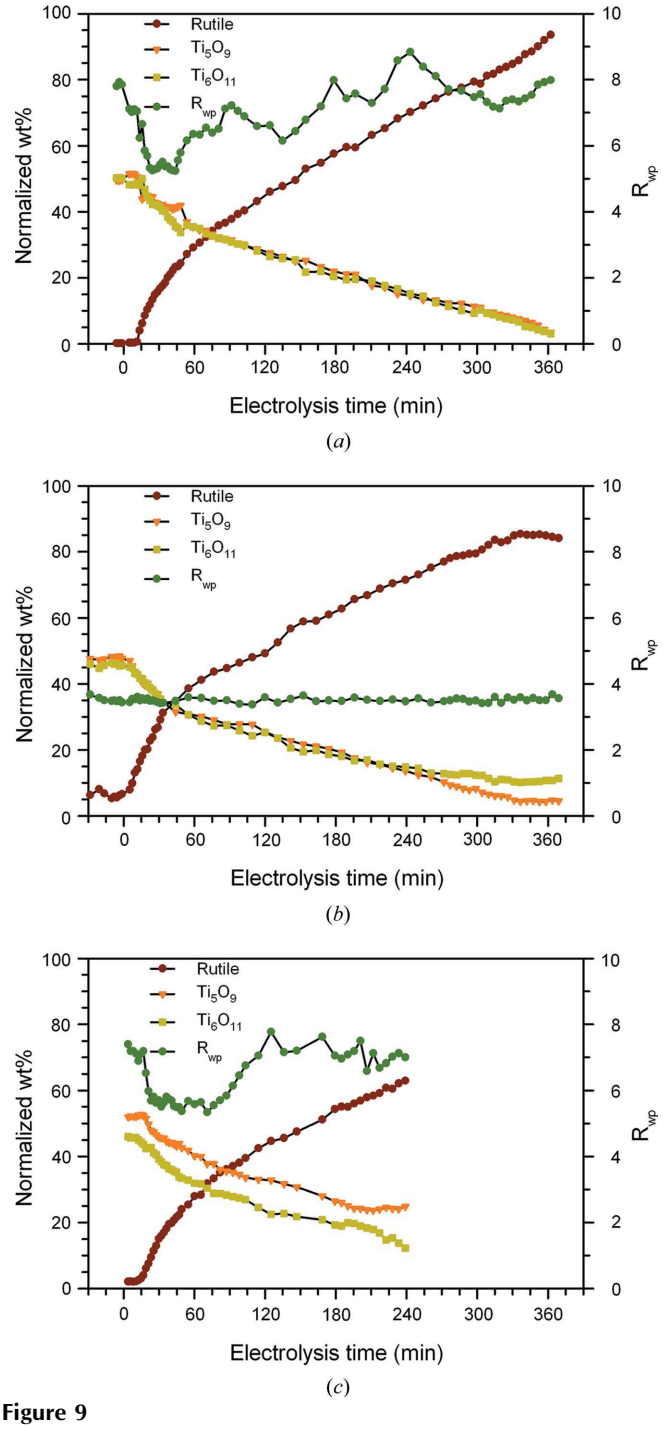

Figure 9
Results of quantitative phase analysis from data collected (*a*) above the melt at full current, (*b*) below the melt at full current and (*c*) above the melt at half current.

rate of solid-state diffusion of oxygen within the anode structure than the amount of oxygen available.

The rutile layer thickness did not follow the linear dependence with time shown previously (Scarlett *et al.*, 2009; Rowles *et al.*, 2011), most likely because of the relatively few data points available in the previous experiment. Although the model shows rutile formation on the anode when immersed in the electrolyte with no current applied to the electrodes (see Fig. 9*b*), it is thought that this may be an artefact arising from the poorer quality data collected from below the melt.

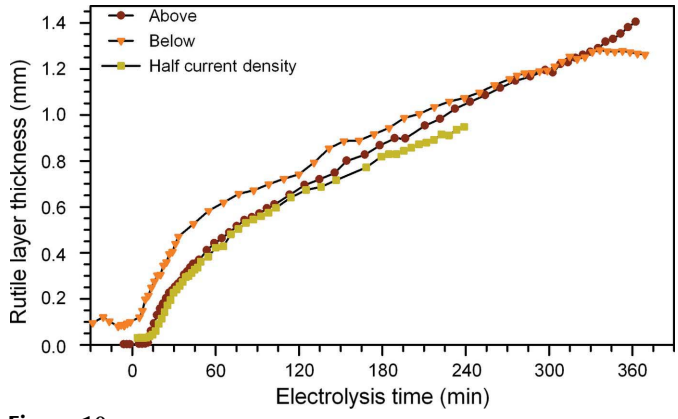

Figure 10
Results of rutile layer thickness calculations [equation (20)].

4. Conclusions

The formation of rutile passivation layers on a Magnéli-phase inert anode has been observed by *in situ* energy-dispersive X-ray diffraction and the data analysed and quantified *via* the Rietveld (1969) method. The only phases observed in the three anodes were rutile and the Magnéli phases Ti_5O_9 and Ti_6O_{11}. The analysis method as implemented by Scarlett *et al.* (2009) has been extended to include the contributions from crystallite size and strain, fluorescence, detector escape peaks and the Lorentz factor.

The resultant rutile layer thickness has been calculated and it is thought that, because of the similarity between the layer growth at full and half current, the limiting factor in the growth of the rutile layer is the rate of solid-state diffusion of oxygen within the anode structure. The continual monitoring of the rutile thickness throughout the duration of the experiment revealed the way in which the layer grows, something that would be very difficult to do accurately *via ex situ* experimentation.

The similarities in the quantitative phase analysis both above and below the melt suggest that it is possible to obtain meaningful *in situ* diffraction data with the incident beam just above the melt surface, mitigating the deleterious effect of X-ray absorption on the resultant diffraction patterns.

The furnace and electrochemical cell design directly allows for the investigation of changes in the anode or cathode of molten salt electrolyses. Furthermore, the design is flexible enough to allow for custom inserts to be produced to investigate materials in a variety of atmospheres at temperatures up to 1373 K by either energy-dispersive or high-energy monochromatic X-ray diffraction.

We acknowledge travel funding provided by the International Synchrotron Access Program (ISAP) managed by the Australian Synchrotron. The ISAP is an initiative of the Australian Government being conducted as part of the National Collaborative Research Infrastructure Strategy. We

thank Diamond Light Source for access to beamline I12 – Joint Engineering, Environmental and Processing (EE3171) – which contributed to the results presented here. We would like to thank Principal Beamline Scientist Dr Michael Drakopolous and his team for providing a most excellent instrument. This work was conducted as part of doctoral studies undertaken through the University of Melbourne. MJS gratefully acknowledges receipt of a full PhD scholarship from the CSIRO Flagship Collaboration Fund, and additional funding from the CSIRO Light Metals Flagship which has made this work possible.

References

Andersson, S., Collen, B., Kuylenstierna, U. & Magnéli, A. (1957). *Acta Chem. Scand.* **11**, 1641–1652.
Azároff, L. V. (1955). *Acta Cryst.* **8**, 701–704.
Barnes, P., Colston, S., Craster, B., Hall, C., Jupe, A., Jacques, S., Cockcroft, J., Morgan, S., Johnson, M., O'Connor, D. & Bellotto, M. (2000). *J. Synchrotron Rad.* **7**, 167–177.
Bruker (2009). *TOPAS*. Version 4.2. Bruker AXS, Karlsruhe, Germany.
Cernik, R. J., Hansson, C. C. T., Martin, C. M., Preuss, M., Attallah, M., Korsunsky, A. M., Belnoue, J. P., Jun, T. S., Barnes, P., Jacques, S., Sochi, T. & Lazzari, O. (2011). *J. Appl. Cryst.* **44**, 150–157.
Fray, D. J. (2008). *Int. Mater. Rev.* **53**, 317–325.
Gerward, L., Mørup, S. & Topsøe, H. (1976). *J. Appl. Phys.* **47**, 822–825.
Gianatta, M. V. (2000). *JOM*, **52**, 18–20.
Giessen, B. C. & Gordon, G. E. (1968). *Science*, **159**, 973–975.
Habashi, F. (1997). *Handbook of Extractive Metallurgy*. Weinheim: Wiley-VCH.
Häusermann, D. & Barnes, P. (1992). *Phase Transitions*, **39**, 99–115.
Hayfield, P. C. S. (1983). US Patent 4 422 917.
Hill, R. J. & Howard, C. J. (1987). *J. Appl. Cryst.* **20**, 467–474.
Hubbell, J. H. & Seltzer, S. M. (2004). *Tables of X-ray Mass Attenuation Coefficients and Mass Energy-Absorption Coefficients from 1 keV to 20 MeV for Elements Z = 1 to 92 and 48 Additional Substances of Dosimetric Interest*, NIST Standard Reference Database 126, http://www.nist.gov/pml/data/xraycoef/index.cfm.
Jiao, S. & Fray, D. J. (2010). *Metall. Mater. Trans. B*, **41**, 74–79.
Kortright, J. B. & Thompson, A. C. (2001). *X-ray Emission Energies, X-ray Data Booklet*, edited by A. C. Thompson & D. Vaughan. Berkeley: Lawrence Berkeley National Laboratory.
Kraft, E. H. (2004). *Summary of Emerging Titanium Cost Reduction Technologies.* EHK Technologies.
Kroll, W. (1940). *Trans. Am. Electrochem. Soc.* **78**, 35–47.
Lange, J. (1995). *Acta Cryst.* A**51**, 559–565.
Le Page, Y. & Strobel, P. (1982*a*). *J. Solid State Chem.* **43**, 314–319.
Le Page, Y. & Strobel, P. (1982*b*). *J. Solid State Chem.* **44**, 273–281.
Madsen, I. C., Scarlett, N. V. Y., Cranswick, L. M. D. & Lwin, T. (2001). *J. Appl. Cryst.* **34**, 409–426.
McGregor, K., Frazer, E. J., Urban, A. J., Pownceby, M. I. & Deutscher, R. L. (2006). *ECS Trans.* **2**, 369–380.
McGregor, K., Urban, A. J. & Frazer, E. J. (2007). *Proceedings of the 11th World Conference on Titanium*, edited by M. Niinomi, S. Akiyama, M. Hagiwara, M. Ikeda & K. Maruyama, pp. 127–130. Sendai: The Japan Institute of Metals.
Pawlek, R. P. (2008). *Inert Anodes: An Update, Light Metals 2008*, pp. 1039–1045. Warrendale: Minerals, Metals and Materials Society.
Pawlek, R. P. (2010). *Wettable Cathodes: An Update, Light Metals 2010*, pp. 377–382. Warrendale: Minerals, Metals and Materials Society.
Restori, R., Schwarzenbach, D. & Schneider, J. R. (1987). *Acta Cryst.* B**43**, 251–257.
Rietveld, H. M. (1969). *J. Appl. Cryst.* **2**, 65–71.
Rowles, M. R. (2011). *J. Synchrotron Rad.* **18**, 938–941.
Rowles, M. R., Scarlett, N. V. Y., Madsen, I. C. & McGregor, K. (2011). *J. Appl. Cryst.* **44**, 853–857.
Russenbeek, J., Gao, Y., Zhong, Z., Croft, M., Jisrawi, N., Ignatov, A. & Tsakalakos, T. (2011). *J. Power Sources*, **196**, 2332–2339.
Sánchez Del Río, M. & Dejus, R. J. (1997). *Proc. SPIE*, **3152**, 148–157.
Scarlett, N. V. Y., Madsen, I. C., Cranswick, L. M. D., Lwin, T., Groleau, E., Stephenson, G., Aylmore, M. & Agron-Olshina, N. (2002). *J. Appl. Cryst.* **35**, 383–400.
Scarlett, N. V. Y., Madsen, I. C., Evans, J. S. O., Coelho, A. A., McGregor, K., Rowles, M., Lanyon, M. R. & Urban, A. J. (2009). *J. Appl. Cryst.* **42**, 502–512.
Snook, G. A., McGregor, K., Urban, A. J. & Lanyon, M. R. (2009). *J. Solid State Electrochem.* **13**, 591–598.
Stinton, G. W. & Evans, J. S. O. (2007). *J. Appl. Cryst.* **40**, 87–95.
Styles, M. J., Rowles, M. R., Madsen, I. C., McGregor, K., Urban, A. J., Snook, G. A., Scarlett, N. V. Y. & Riley, D. P. (2012). *J. Synchrotron Rad.* **19**, 39–47.
Tzeng, H. S., Ishi, K. & Kamiya, M. (1976). *Chin. J. Phys.* **13**, 47–49.
Young, R. A. (1993). *The Rietveld Method*, edited by R. A. Young, pp. 1–38. New York: Oxford University Press Inc.